Chemistry of Smart Energy Carriers and Technologies

3D-CFD SIMULATIONS OF FUEL SPRAY BREAKUP UNDER NON-EVAPORATING, EVAPORATING AND REACTIVE FLOW CONDITIONS FOR MARINE ENGINE APPLICATIONS

Mr. Xenakis Vouvakos

PhD Candidate

Home Institution:

Division of Marine Engineering
School of Naval Architecture and Marine Engineering
National Technical University of Athens

Host Institution:

Frederick University
Department of Mechanical Engineering

Contents

1. General Issues

1.1. Acronyms and Definitions

Acronym	Definition
CAB	Cascade Atomization and drop Breakup model
CFD	Computational Fluid Dynamics
DI	Direct Injection
ETAB	Enhanced Taylor Analogy Breakup model
IDSD	Initial Droplet Size Distribution
KHRT	Kelvin-Helmholtz – Rayleigh-Taylor
LFO	Light Fuel Oil
RANS	Reynolds Averaged Navier-Stokes
ROHR	Rate Of Heat Release
CVSCC	Constant Volume Spray Combustion Chamber
SMD	Sauter Mean Diameter
SOI	Start Of Injection
TAB	Taylor Analogy Breakup model
TDC	Top Dead Center
3D	Three-Dimensional

2. Scope and summary

Marine Diesel engines are DI engines, since the introduction of fuel into the combustion chamber is via fuel sprays, injected at high pressure. Spray-induced turbulence drives fuel-air mixing; to this end, an effective atomization of the spray jet is essential, in order to increase the surface area of the liquid phase, for rapid evaporation and combustion. Thus, spray dynamics significantly affect ignition, heat release and pollutant formation rates, and is therefore crucial in terms of fuel consumption and exhaust emissions.

3D–CFD numerical simulation of spray dynamics is an integral part of engine research, critical in terms of enhancing our understanding of in-cylinder processes and optimizing combustion. In this context, implementing into CFD codes and properly adapting physical models for spray breakup, evaporation, ignition and combustion is essential.

A major challenge concerning spray modelling with respect to large two-stroke marine Diesel engines is that, due to the higher values of orifice diameter, the values of non-dimensional parameters affecting the dynamics (Weber and Reynolds numbers) are significantly higher than those corresponding to the conditions of smaller engines, for which spray breakup models are commonly optimized. Thus, studying the effect of these parameters in the regime relevant for marine engine applications is essential for understanding the spray dynamics and optimizing spray models for CFD studies of marine Diesel engine aerothermochemistry. In the frame of the present work, CFD spray simulations have been carried out in order to analyze the effects of non-dimensional parameters, in the context of state-of-the-art spray breakup models; namely the CAB and KHRT; both valid for high velocities. The CAB model implemented in KIVA-3V release 2 CFD code has been validated and adapted under a wide range of flow conditions; including non-reactive and reactive spray flows, and the KHRT originally implemented in STAR-CD CFD code has been validated and adapted under non-reactive, non-evaporating conditions. The computational results have been compared with experimental measurements from the unique CVSCC facility installed at Winterthur Gas and Diesel Ltd. Overall, a very good agreement between experiments and the present computational results is demonstrated, both for non-reactive and reactive spray flows. Further, two surrogate diesel fuels, the n-tetradecane ($C_{14}H_{30}$) and n-dodecane ($C_{12}H_{26}$) have been used for CFD spray simulations as representatives for marine LFO. The computational results indicated that both surrogate diesel fuels are appropriate for CFD studies of marine Diesel engine applications.

3. Technical context

3.1. Description of work performed

3.1.1. CFD Codes

3D-CFD simulation can substantially contribute to understand and optimize engine aerothermochemistry. The detailed investigation of in-cylinder processes present in marine diesel engines requires an understanding of several flow and combustion processes. CFD engine simulations commonly involve the numerical solution of RANS conservation equations for mass, momentum and energy [1], [2]. In the present work, KIVA-3V release 2 and STAR-CD CFD codes have been used; both constitute powerful CFD platform for the numerical calculation of transient two- and three-dimensional chemically reactive fluid flows interacting with fuel sprays [3], [4], [5], [6].

In the present fuel spray simulations, the standard collision and evaporation models of KIVA-3V release 2 and STAR-CD codes are utilized [7], [6]. Turbulence is modeled by means of the k-ε RNG turbulence model, with standard values for the model constants [5], [6]. In the present simulations of reactive flow, ignition is modeled in terms of the progress variable ignition model introduced in [8]. Here, a transport conservation equation is solved for a properly defined quantity, the progress variable, which governs the ignition delay and serves as the ignition criterion. The ignition progress variable is a non-dimensional quantity, defined as the concentration of an intermediate species divided by a critical value. Modeling of the overall ignition delay is based on a detailed chemistry mechanism for n-heptane, utilizing a simplified system of characteristic times computed from Arrhenius type correlations. A computed value of the ignition progress variable greater than unity signals ignition for the corresponding computational cell, and activates the combustion model. In the present work, combustion modeling utilizes the characteristic time model introduced in [9].

3.1.2. Spray Modeling

Spray modeling of small engine applications has commonly relied on the TAB and WAVE models [10], [11]. The TAB model is based on an analogy between an oscillating drop penetrating into a gas and a forced damped spring-mass oscillator. The WAVE model is based on the development of KH instabilities on the liquid jets. Experience from the use of TAB in marine engine applications by the NTUA-DME team has shown that it can be associated with high evaporation rates and short ignition delay times, resulting in high ROHR and elevated pressure levels. Thus, an improvement of TAB, the CAB model [12] has been considered in the present study. The CAB model constitutes an extension of the ETAB model [13], [14]. In comparison to TAB, the CAB model includes a power law for the Initial Droplet Size Distribution (IDSD), accounting for spray jet stripping near the nozzle. A realistic prediction of ratios of child to parent droplet radius is attained by considering that the initially injected drops at the nozzle are characterized by a negative deformation velocity; this properly accounts for the existence of a liquid core, and extends the droplet lifetime. The KHRT model combines the effects of Kelvin-Helmholtz waves driven by aerodynamic forces with Rayleigh-Taylor instabilities due to acceleration of shed drops ejected into free stream conditions; both mechanisms model droplet breakup by tracking wave growth on the surface of the droplet, with breakup occurring due to the fastest growing instability based on local conditions [15]. The

KHRT and CAB breakup models are valid for high velocity sprays, accounting for the catastrophic secondary breakup [1], [2].

3.1.3. Experimental Data and Test Cases

Experimental data available from the CVSCC facility installed at Winterthur Gas and Diesel Ltd. [16] have been used for model validation. The CVSCC is a unique experimental facility, which enables the investigation of in-cylinder processes such as fuel injection and evaporation, ignition, combustion and emission formation, at conditions close to those of large two-stroke marine diesel engines [17]. Thus, valuable experimental data can validate and support the development of CFD models, to be used in studying and optimizing flow and combustion in marine engines.

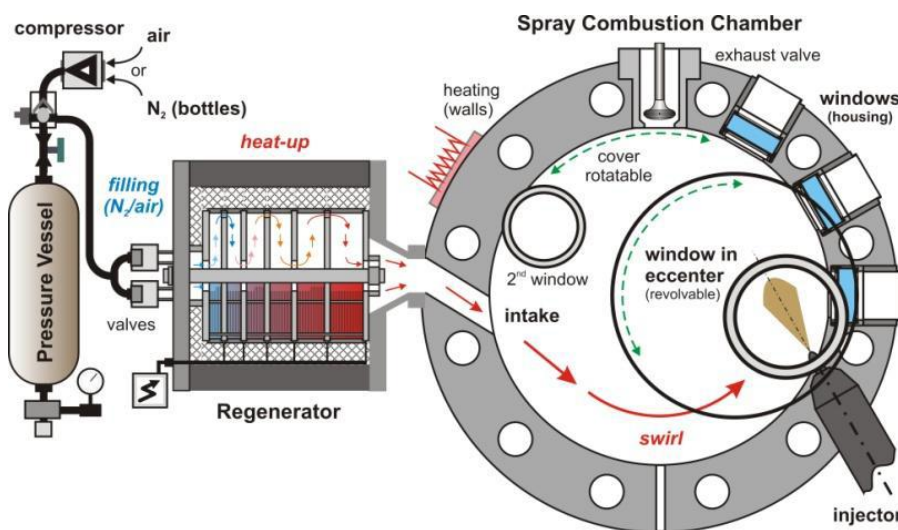Figure 1 presents a schematic of the SCC facility.

Figure 1: Schematic of the SCC facility [17].

This optically accessible chamber has a disk shape, with a diameter of 500 mm and a height of 150 mm. Fuel is injected from the chamber periphery, at its mid-plane, into swirling air or nitrogen (N_2). At the Start Of Injection (SOI), realistic operating conditions (up to 13 MPa, 930 K) are achieved by feeding the chamber via inclined intake channels with pressurized and heated gas provided by pressure vessels connected to a heat regenerating device. The tilted intake provides the desired swirl motion, which at SOI can be approximated by a solid body rotation, with a velocity of 20 m/s at a radial position of 200 mm [17].

CFD spray simulations by using the CAB model for both evaporating and non-evaporating non-reactive conditions, utilizing n-tetradecane ($C_{14}H_{30}$) properties to represent LFO, have been performed with KIVA code. The non-evaporating as well as the evaporating cases correspond to conditions and injection characteristics utilized in the experimental studies of [16]. Further, reactive spray simulations have been carried out. In the non-reactive (non-evaporating and evaporating) cases, densities of the surrounding gas (nitrogen) of 11.2, 22.5 and 33.7 kg/m^3 have been considered, and the results have been validated against the experiments reported in [16], in terms

of spray penetration length and cone angle. The high gas density of 33.7 kg/m^3 under evaporating (non-reactive) spray conditions has been selected for model adaptation. Finally, reactive spray simulations have been performed, for a surrounding air density of 34.5 kg/m^3.

The lower gas density of 11.2 kg/m^3 under non-evaporating (non-reactive) spray condition has been selected for spray simulations with n-dodecane ($C_{12}H_{26}$) as representative for marine LFO. Here, CFD spray simulations with both spray breakup models; the CAB and KHRT have been carried out, by using KIVA and STAR-CD CFD codes respectively.

A swirling gas flow has been considered at SOI, with velocities prescribed in terms of a Bessel function, corresponding to a solid body swirl angular velocity of 100 rad/s. The cases computed are summarized in Table 1, while important input data are presented in Table 2.

Filling gas: nitrogen (N$_2$) – non-reactive flow							Filling gas: air – reactive flow
Case	1	2	3	4	5	6	7
Gas temperature [K]	400 (non-evaporating)			900 (evaporating)			915 (evaporating)
Gas pressure [bar]	13	27	40	30	60	90	91
Gas density [kg/m^3]	11.2	22.5	33.7	11.2	22.5	33.7	34.5
Swirl angular velocity [rad/s]	100 (Bessel function profile)						

Table 1: Cases computed in the present work.

Number of nozzle holes	1
Diameter of nozzle hole [mm]	0.875
Injection pressure [bar]	1000
Injector nozzle orientation	co-swirl
$C_{14}H_{30}$ / $C_{12}H_{26}$ temperature [K]	323
Wall temperature [K]	453

Table 2: Simulation input data.

3.1.4. Computational Grid

The ANSYS module ICEM-CFD has been used for grid generation. It is a state-of-the-art meshing tool able to generate both structured and unstructured grids. The ICEM-CFD has an interface for output in a format required by KIVA and STAR-CD CFD codes [18].

A finite volume mesh has been used to discretize the domain considered in the present work, i.e. the disk-shaped of CVSCC [17], [19]. Taking into account the large size of the chamber, grid generation has aimed at effective block-structured meshes, for adequately resolving the spray regime, while maintaining a reasonable computational cost [3]. The investigation converged to a twenty seven block grid. Figure 2 shows the front and bottom views of a grid used in the present work. Different grid densities have been tested, characterized by cells of 4X4 mm, 5X5 mm and 6X6 mm. Information regarding the three grids utilized in the present spatial resolution studies is reported in Table 3.

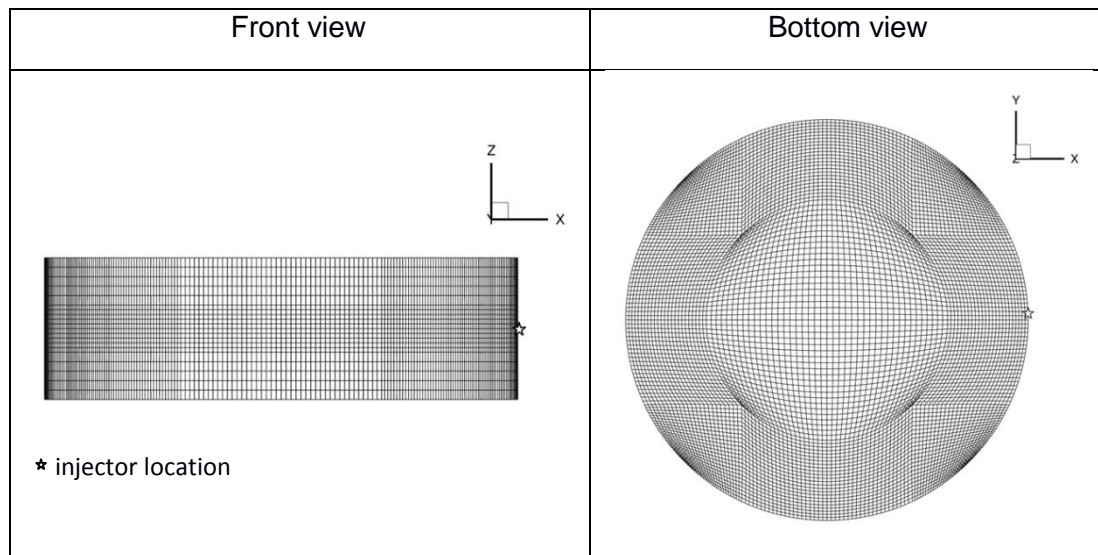| Front view	Bottom view
* injector location	

Figure 2: Front and bottom views of a grid used in the present SCC simulations.

Mesh (Ø500x150 mm)	Number of cells	Spray regime resolution
Coarse	110,000	6 mm
Fine	180,000	5 mm
Very fine	250,000	4 mm

Table 3: Features of the computational grids used in spatial resolution tests.

3.2. Results

3.2.1. Spray Models Adaptation

Adaptation of the CAB spray model was performed for operating conditions corresponding to Case 6 presented in Table 1, using the fine mesh of Table 3. Case 6 is perceived as a demanding one, as it involves both breakup and evaporation, while it corresponds to conditions similar to those of marine diesel engines. A good agreement between the computed and measured time history of penetration length was used as the main criterion for adapting the spray model. It is noted that, in adapting the spray model, the value of the initial spray angle, which depends on the gas density, is prescribed based on the experimental measurements reported in [16]. Further, the computational results are analyzed in terms of visualization of the flow field. The optimal constant values obtained are reported in Table 4; these values were maintained for all other cases computed.

The KHRT spray model was adapted only under non-evaporating conditions. In particular, adaptation was performed for operating conditions corresponding to Case 1 presented in Table 1, utilizing the fine mesh of Table 3. The quantitative criteria for model adaptation were the spray penetration length and the cone angle. As in CAB model adaptation the value of the initial spray angle, which depends on the gas density, is prescribed based on the experimental measurements reported in [16]. The computational results are analyzed in terms of visualization of the flow field and the optimal constant values obtained are reported in Table 5.

Constant	Description	Default	Range tested	Outcome
θ	Initial spray angle [deg.]	20 ~ 25	10 – 16	10 ~ 16
C_λ	Nozzle dependent constant	5.5	1.0 - 30.0	11.0
k_1	Time scale parameter for bag break-up	0.05	0.01 – 0.25	0.1
k_2	Time scale parameter for stripping break-up	Calculated based on k_1	Calculated based on k_1	Calculated based on k_1
k_3	Time scale parameter for catastrophic break-up	Calculated based on k_1	Calculated based on k_1	Calculated based on k_1
n	Exponent in IDSD	0.5	0.1 – 1.5	1.0

Table 4: Optimal values of the CAB model constants, obtained for conditions corresponding to Case 6.

Constant	Description	Default	Range tested	Outcome
KHB_0	Kelvin-Helmholtz model constant	0.61	0.51 – 0.71	0.61
KHB_1	Kelvin-Helmholtz model time constant	40	1.0 – 60	1.0
RTC_3	Rayleigh-Taylor model size constant	0.1	0.1 – 0.11	0.1
RTC_t	Rayleigh-Taylor model time constant	1.0	1.0 – 11.0	2.0

Table 5: Optimal values of the KHRT model constants, obtained for conditions corresponding to Case 1.

3.2.2. Resolution Tests

Both spatial and temporal resolution tests have been performed using the CAB model, in order to investigate the dependence of computational results on discretization parameters. First, spatial resolution tests were performed, utilizing the three grids presented in Table 3, for Case 3. The computational time step was in all cases $\Delta t=10^{-5}$ s. Figure 3 shows the calculated time history of the spray penetration length for all three grids, which is compared with the corresponding experimental data of [16]. An increase of penetration length is observed for increased resolution. In general, there is very good agreement between the present CFD results and the experiment. For all grids, the results coincide in the initial stage of injection, and are very close to the experimental curve. Subsequently, there are small differences in the computed values of penetration length; these differences are minimal for the two fine grids.
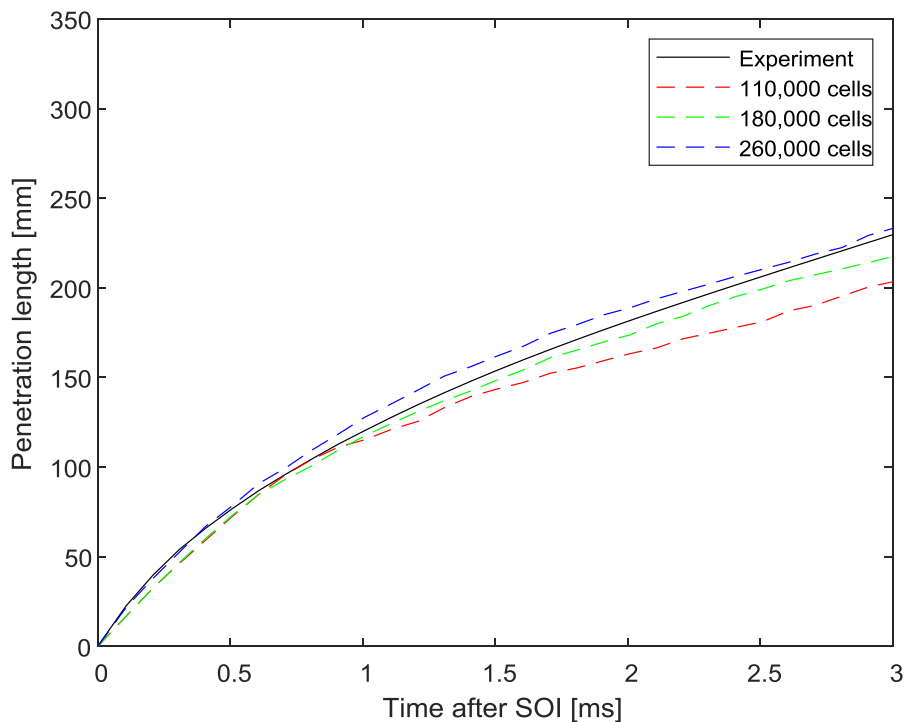

Figure 3: Case 3: calculated penetration length versus time for the three computational grids considered. The time step value is $\Delta t=10^{-5}$ s. The corresponding experimental curve of [16] is also included.

As the very fine mesh (~260,000 cells) is characterized by quite high computational cost, while giving results only slightly deviating from the fine mesh (~180,000 cells), the latter is selected for the subsequent computational simulations.

Finally, Case 3 was computed for different time step values using the fine mesh. These temporal time resolution tests involved time step values ranging from 10^{-6} s to 10^{-4} s. Minimal variations in spray penetration length were observed for time steps lower than 10^{-5} s. Thus, a numerical time step of $\Delta t=10^{-5}$ s was selected for the subsequent computations.

3.2.3. Non-Evaporating Spray Simulations

Figure 4 shows the calculated time history of the spray penetration length, for Case 1 using the CAB and the KHRT models with n-dodecane ($C_{12}H_{26}$) as representative for marine LFO. The results are compared with the corresponding experimental data of [16], and with the computed spray penetration length, utilizing the CAB model with n-tetradecane ($C_{14}H_{30}$) properties to represent LFO. An overall good agreement is observed. The results illustrate that the penetration lengths computed with n-dodecane ($C_{12}H_{26}$) are higher than this of n-tetradecane ($C_{14}H_{30}$). This trend is justified by the fact that the n-dodecane ($C_{12}H_{26}$) is lighter than the n-tetradecane ($C_{14}H_{30}$).
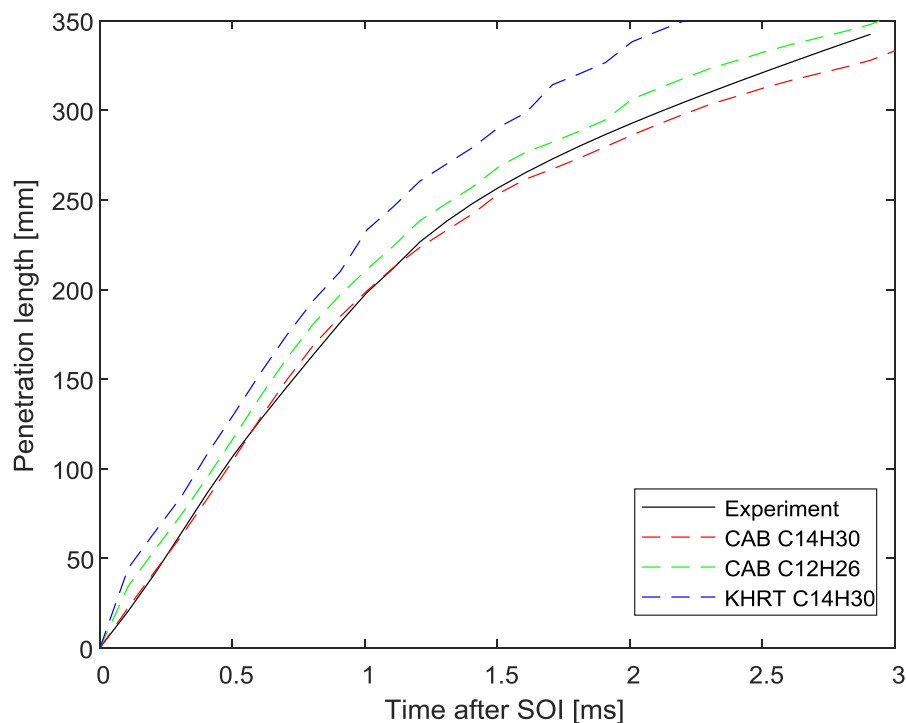

Figure 4: Computed time history of spray penetration length, for Case 1, which correspond to gas density of 11.2 kg/m^3 using the CAB and KHRT models with n-dodecane ($C_{12}H_{26}$) as representative for marine LFO. The corresponding experimental curves of [16] are also included as well as the computed time history of spray penetration length utilizing the CAB model with n-tetradecane ($C_{14}H_{30}$) properties to represent LFO.

Figure 5 presents snapshots of droplets velocity, at representative times (up to 3 ms after SOI), for Case 1 using the CAB and the KHRT models with n-dodecane ($C_{12}H_{26}$) and the CAB with n-tetradecane ($C_{14}H_{30}$); here, the horizontal plane including the injector is considered. The present results demonstrate a slightly higher propagation of the spray with n-dodecane ($C_{12}H_{26}$).
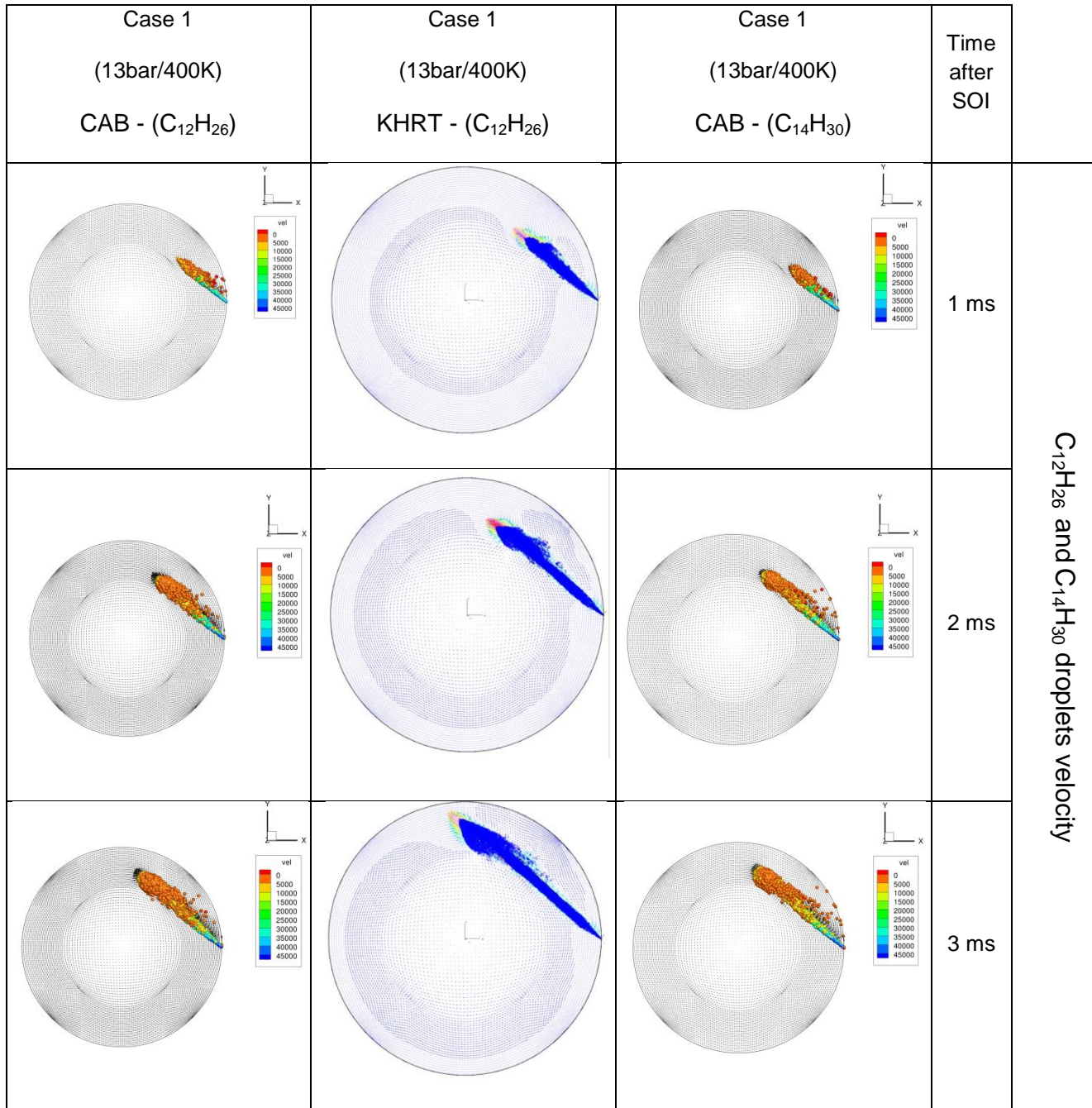
Case 1 (13bar/400K) CAB - ($C_{12}H_{26}$)	Case 1 (13bar/400K) KHRT - ($C_{12}H_{26}$)	Case 1 (13bar/400K) CAB - ($C_{14}H_{30}$)	Time after SOI	
			1 ms	
			2 ms	$C_{12}H_{26}$ and $C_{14}H_{30}$ droplets velocity
			3 ms	

Figure 5: Color-coded contours of gas velocity at the horizontal plane including the injector, at representative time instants after SOI for Case 1.

Figure 6 presents the computed spray penetration length versus time, for Case 1, Case 2 and Case 3 using the CAB model; the experimental curves of [16] are also presented. An overall very good agreement is observed. The results illustrate the strong impact of gas density on spray development, as the penetration length is significantly lower at higher gas density. The trend is justified by the fact that the fuel spray experiences higher aerodynamic forces, resulting in higher values of Weber number.
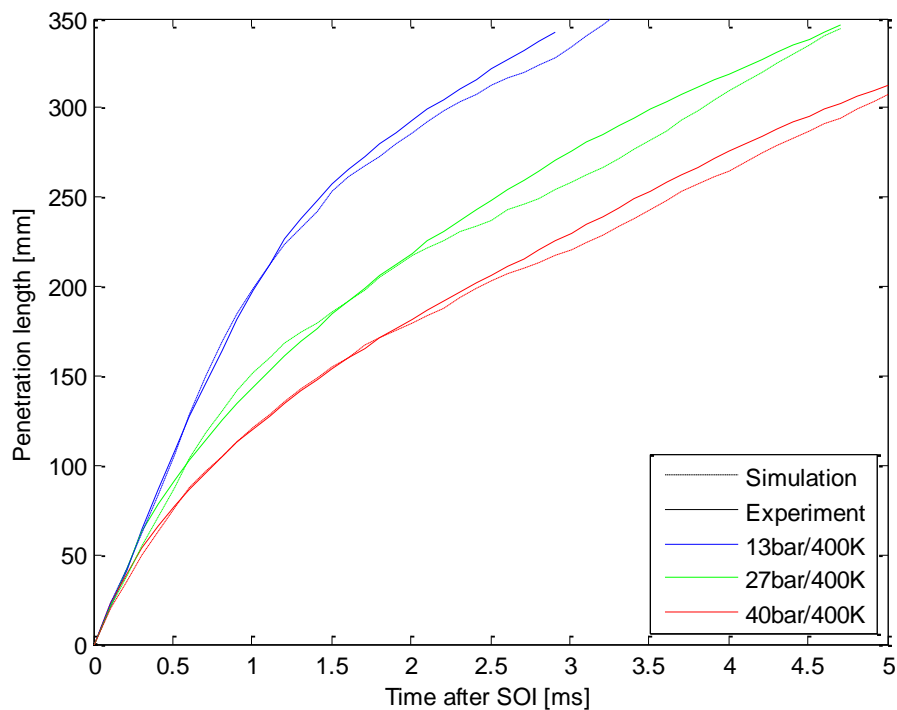
Figure 6: Computed time history of spray penetration length, for Case 1, Case 2, and Case3, which correspond to gas density of 11.2 kg/m^3, 22.5 kg/m^3 and 33.7 kg/m^3, respectively. All cases are characterized by a strong swirling gas flow. The corresponding experimental curves of [16] are also included.

Figure 7 presents snapshots of droplets velocity, at representative times (up to 3 ms after SOI), for Case 1, Case 2 and Case 3; here, the horizontal plane including the injector is considered. The present results demonstrate a substantially slower propagation of the spray at high gas density (Case 3), due to higher values of Weber number, resulting in enhanced breakup, in accordance with the trends of Figure 6. The effect of the swirling gas motion on spray structure is also evident.
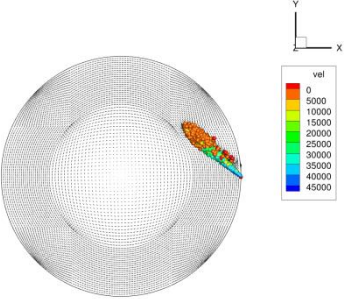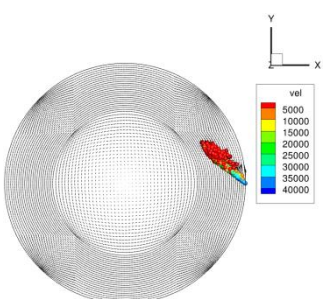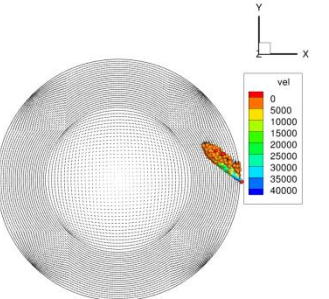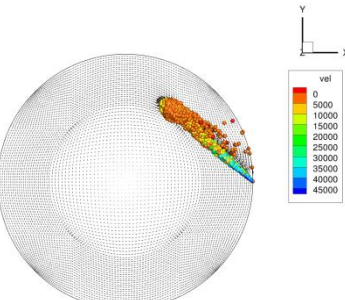
WG5: Integration of fundamental knowledge towards
technology application for Smart Energy Carriers
exploitation

12 of 23
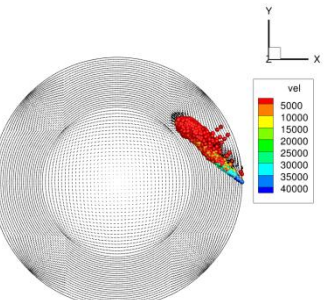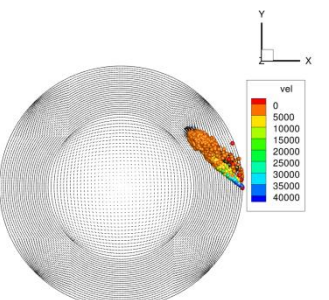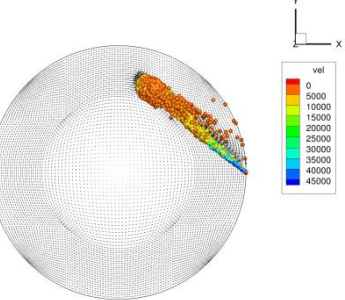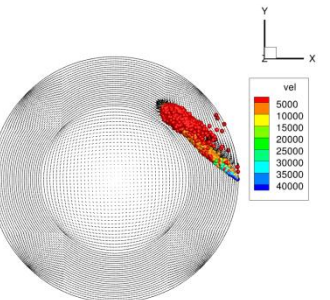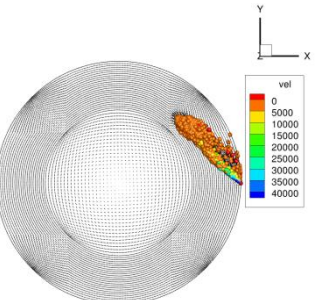
Case 1 (13bar/400K)	Case 2 (27bar/400K)	Case 3 (40bar/400K)	Time after SOI	
			1 ms	C₁₄H₃₀ droplets velocity
			2 ms	
			3 ms	

Figure 7: Color-coded contours of droplets velocity at the horizontal plane including the injector, at representative time instants after SOI for Case 1, Case 2 and Case 3.

3.2.4. Effect of Swirl

Figure 8 illustrates the impact of gas swirling flow on spray penetration length for Case 3, which is characterized by a surrounding gas density value 33.7 kg/m^3 (and co-swirl injection). The effect of swirl evidently increases the penetration length, in agreement with experimental observations [16].
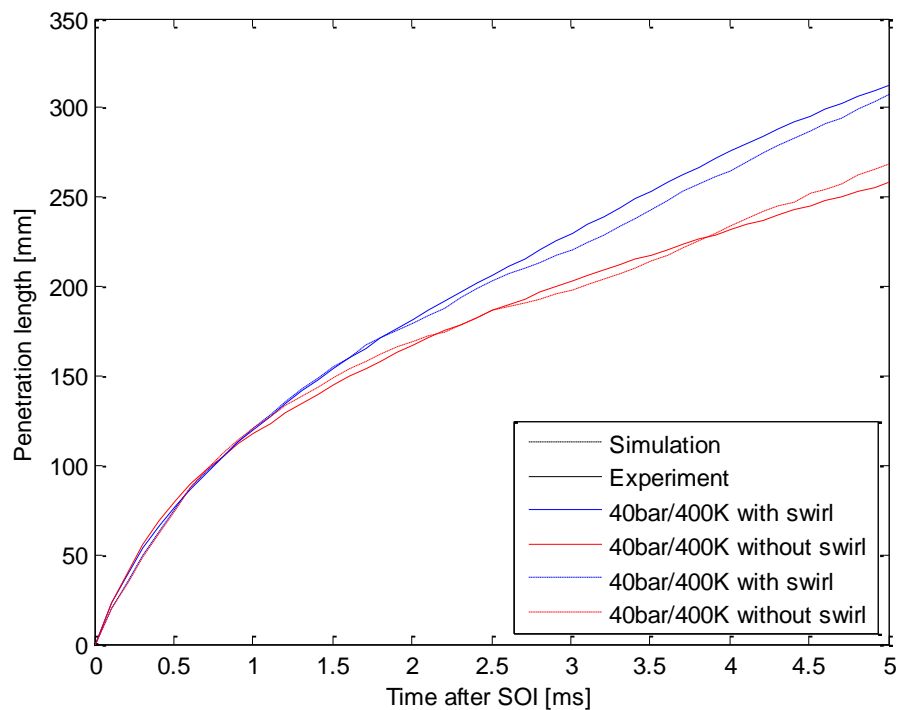
Figure 8: Case 3: computed time history of spray penetration length, with and without swirling gas flow in the SCC. The corresponding experimental curves of [16] are also included

Figure 9 presents snapshots of droplets velocity at representative times (up to 3 ms after SOI); the plane including the injector is considered. During the injection event, the velocity flow field in front of the injector nozzle exit does not differ substantially between the two cases, since the same mass injection profile is used, and the spray jet formed constitutes the prevailing factor for generating high velocity levels in the gas flow.

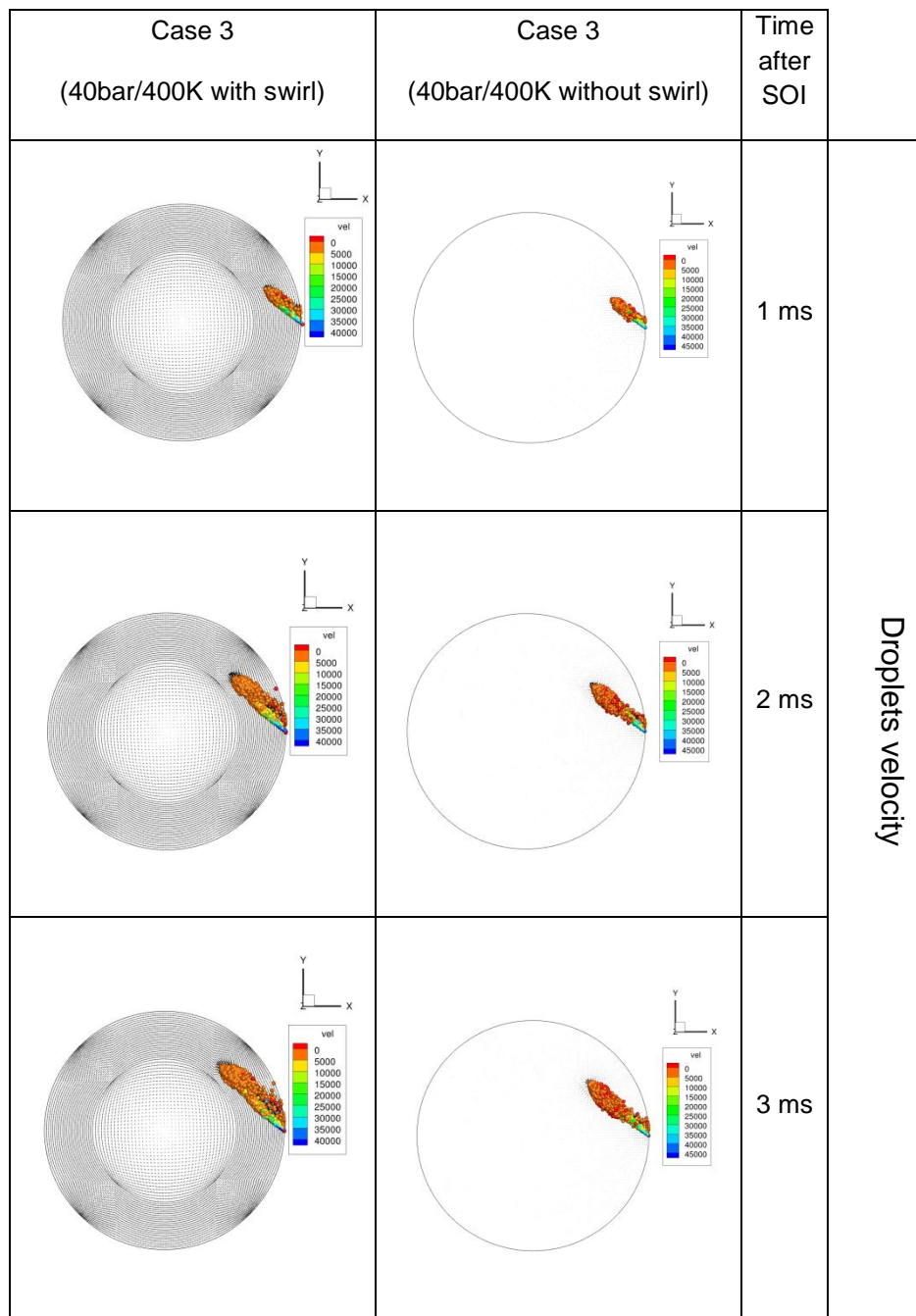| Case 3 (40bar/400K with swirl)	Case 3 (40bar/400K without swirl)	Time after SOI	
		1 ms	
		2 ms	Droplets velocity
		3 ms	

Figure 9: Color-coded contours of droplets velocity at a plane including the injector, for Case 3 (swirling gas flow) and a corresponding case with no swirl, at representative time instants after SOI.

3.2.5. Evaporating Spray Simulations

Figure 10 presents the computed spray penetration length versus time under evaporating conditions, in particular, for Case 4, Case 5 and Case 6 using the CAB model; the experimental curves of [16] are also presented. A good agreement is observed. As in the non-evaporating cases considered, the results illustrate the strong impact of gas density on spray development, as the penetration length is significantly lower of the higher gas density. The trend is justified by the fact

WG5: Integration of fundamental knowledge towards
technology application for Smart Energy Carriers
exploitation

15 of 23

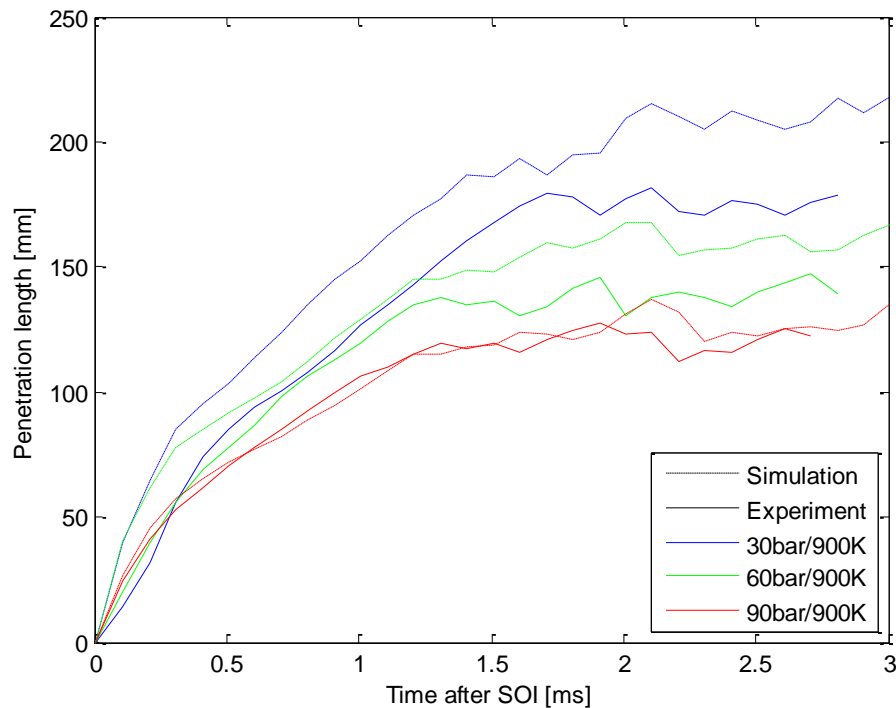that the fuel spray experiences higher aerodynamic forces, resulting in higher values of Weber number.

Figure 10: Computed time history of spray penetration length, for Case 4, Case 5, and Case6 using the CAB model, corresponding to gas density of 11.2 kg/m^3, 22.5 kg/m^3 and 33.7 kg/m^3, respectively. All cases are characterized by a strong swirling gas flow. The corresponding experimental curves of [16] are also included.

Figure 11 and Figure 12 present snapshots of droplets velocity and n-tetradecane ($C_{14}H_{30}$) vapor mass fraction, respectively, at representative times (up to 3 ms after SOI), for Case 4, Case 5 and Case 6; here, the horizontal plane including the injector is considered. As in the non-evaporating conditions, the stronger breakup at high pressure is demonstrated by the computed distribution of gas flow velocity. Regarding evaporation, higher evaporation rates are observed at values of pressure.

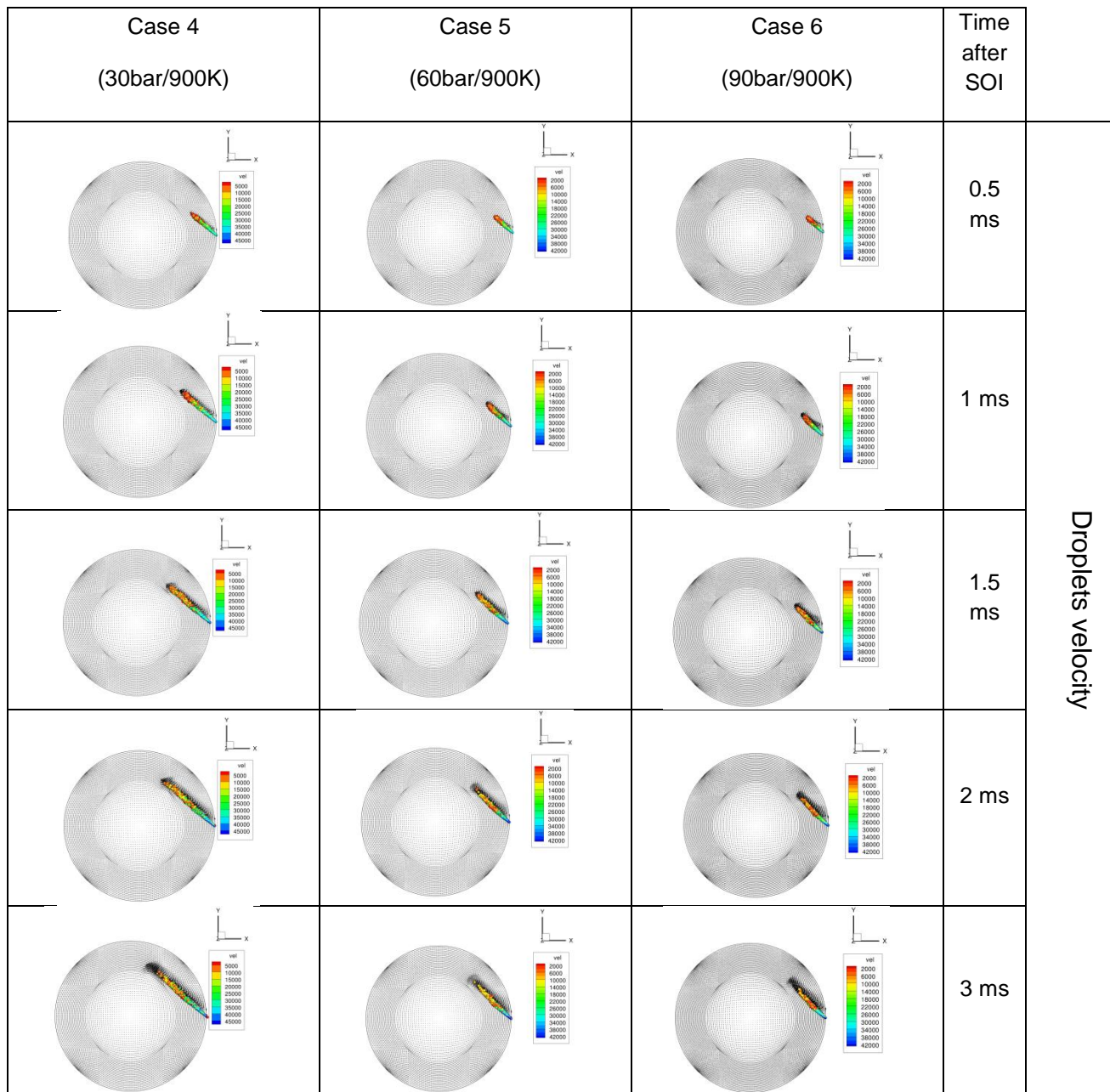| Case 4 (30bar/900K)	Case 5 (60bar/900K)	Case 6 (90bar/900K)	Time after SOI	
			0.5 ms	
			1 ms	Droplets velocity
			1.5 ms	
			2 ms	
			3 ms	

Figure 11: Color-coded contours of gas velocity at the horizontal plane including the injector, at representative time instants after SOI, for Case 4, Case 5 and Case 6.
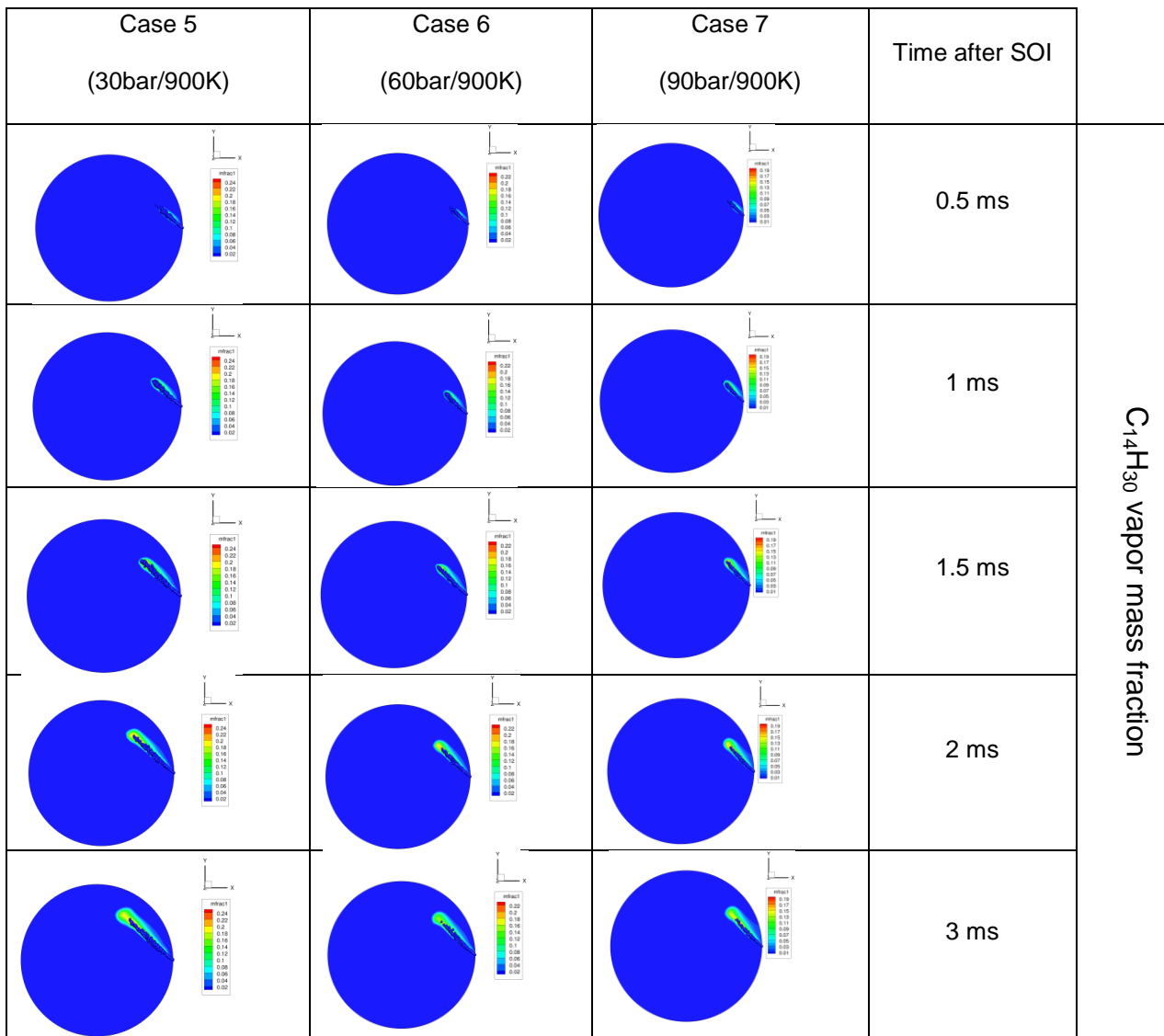
Case 5 (30bar/900K)	Case 6 (60bar/900K)	Case 7 (90bar/900K)	Time after SOI	
			0.5 ms	C$_{14}$H$_{30}$ vapor mass fraction
			1 ms	
			1.5 ms	
			2 ms	
			3 ms	

Figure 12: Color-coded contours of C$_{14}$H$_{30}$ vapor mass fraction at the horizontal plane including the injector, at representative time instants after SOI, for Case 1, Case 2 and Case 3.

3.2.6. Reactive Spray Simulations

Reactive flow has been computed for initial values of air pressure and temperature representative of large two-stroke marine engines at Top Dead Center (TDC), as presented in Table 1 (Case 7). Figure 13 presents snapshots of temperature iso-contours, at representative times after SOI. The overall development of reactive spray flow, including the flame lift-off, is illustrated.
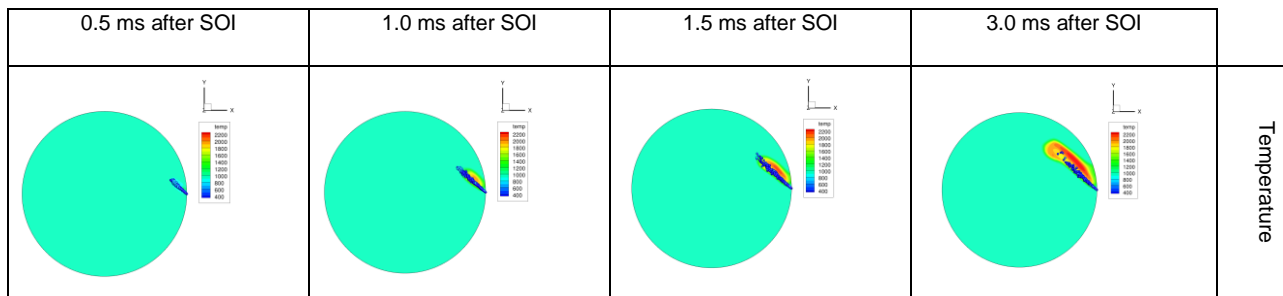
0.5 ms after SOI	1.0 ms after SOI	1.5 ms after SOI	3.0 ms after SOI	

Figure 13: Color-coded contours of temperature at the horizontal plane including the injector, at representative time instants after SOI for Case 7.

4. Conclusions

In the present work the CAB model implemented in KIVA-3V release 2 CFD code has been validated and adapted under a wide range of flow conditions. Detailed simulations have been performed for non-reactive flow, both for non-evaporating and evaporating conditions; a good agreement against experiments in the CVSCC facility has been demonstrated, for a wide range of gas conditions. The KHRT originally implemented in STAR-CD CFD code has been validated and adapted under non-reactive, non-evaporating conditions and an overall very good agreement against experiments in the CVSCC facility has been demonstrated. Further, the preliminary spray simulations performed under non-reactive non-evaporating conditions with the two surrogate diesel fuels; the n-tetradecane (C14H30) and n-dodecane (C12H26) indicated that both are appropriate for CFD studies of marine Diesel engine applications.

5. Future work

The optimized constants of CAB spray breakup model can be used in detailed studies of mixture formation and combustion optimization in large marine Diesel engines, including a proper parameter selection for reducing fuel consumption and pollutant emissions. Further, for engine simulations the KHRT spray breakup model should be validated and adapted under evaporating and reactive conditions.

6. References

[1] **G. Stiesch**, "Modeling Engine Spray and Combustion Processes", Springer edition, Germany, 2006.

[2] **C. Baumgarten**, "Mixture Formation in Internal Combustion Engines", Springer edition, Germany, 2006.

[3] **A.A. Amsden**, "KIVA-3: A KIVA program with block-structured mesh for complex geometries", Los Alamos National Laboratory, LA-12503-MS, 1993.

[4] **A.A. Amsden**, "KIVA-3V: A KIVA program with block- structured mesh for complex geometries", Los Alamos National Laboratory, LA-13313-MS, 1997.

[5] **A.A. Amsden**, "KIVA-3V Release 2: A KIVA program with block-structured mesh for complex geometries", Los Alamos National Laboratory, LA-13608-MS, 1999.

[6] **CD-adapco,** STAR Methodology, STAR-CD Version 4.22, 2014.

[7] **A.A. Amsden**, "KIVA-2: A KIVA program with block-stractured mesh for complex geometries", Los Alamos National Laboratory, LA-12503-MS, 1989.

[8] **G.A. Weisser, F.X. Tanner K. Boulouchos**, "Modeling of Ignition and Early Flame Development with Respect to Large Diesel Engine Simulation", SAE Technical Paper, Series 981451, 1998.

[9] **S.C. Kong, Z. Han, R. Reitz**, "The Development and Application of a Diesel Ignition and Combsution Model for Multidimensional Engine Simulation", SAE Technical Paper, Series 950278, 1995.

[10] **P.J. O'Rourke, A.A. Amsden**, "The TAB Method for Numerical Calculation of Spray Droplet Breakup", SAE Technical Paper, Series 872089, 1987.

[11] **R.D. Reitz,** "Modeling Atomization Process in High-Pressure Vaporizing Sprays", Atomization and Spray Technology, 1987. 3(4):p.309-337.

[12] **F.X. Tanner**, "Development and Validation of a Cascade Atomization and Drop Breakup Model for High-Velocity Dense Sprays", Atomization and Sprays, Vol. 14, pp. 211-242, 2004.

[13] **F.X. Tanner**, "Liquid Jet Atomization and Droplet Breakup Modeling of Non-evaporating Diesel Fuel Sprays", SAE Technical Paper, Series 970050, 1997.

[14] **F.X. Tanner, G.A. Weisser**, "Simulation of Liquid Jet Atomization for Fuel Sprays by means of Cascade Drop Breakup Model", SAE Technical Paper, Series 980808, 1998.

[15] **J.C. Beale, R.D. Reitz,** "Modeling Spray Atomization with the Kelvin-Helmholtz / Rayleigh-Taylor Hybrid Model", Atomization and Sprays, 1999.

[16] **B. v. Rotz, K. Herrman, G.A. Weisser, M. Cattin, M. Bolla, K. Boulouchos**, "Impact of Evaporation, Swirl and Fuel Quality on the Characteristics of Spray Typical of Large 2-Stroke Marine Diesel Engine Combustion Systems", ILASS-Europe, Estoril, Portugal, 2011.

[17] **K. Herrman, R. Schulz, G.A. Weisser**, "Development of a Reference Experiment for Large Diesel Engine Combustion System Optimization", CIMAC Congress, Vienna, Austria, 2007.

[18] **ASNYS Inc,** "ANSYS ICEM CFD User Manual", ANSYS ICEM CFD version 15.0.7, 2015.

[19] **K. Herrman, A. Kyrtatos, R. Schulz, G.A. Weisser, B.v. Rotz. B. Schneider, K. Boulouchos**, "Validation and Initial Application of a Novel Spray Combustion Chamber Representative of Large Two-Stroke Diesel Engine Combustion Systems", ICLASS-America, Colorado, USA, 2009.

7. Appendix 1: The CAB Spray Model

The CAB model [12] constitutes an extension of the ETAB model [13], [14]; both models further improve the TAB model [10]. The CAB model adopts the analogy between an oscillating drop penetrating into a gas (with a given relative velocity) and a forced damped spring-mass system, as in TAB and ETAB (see Figure 14). In particular, the following second order differential equation is considered for drop distortion:

$$\ddot{x} + \frac{d}{m} \cdot \dot{x} + \frac{k}{m} \cdot x = \frac{F}{m} \qquad (1)$$

where, x is the displacement of droplet's equator from its equilibrium state, m is the droplet mass, d is the damping coefficient, k is the spring coefficient, and F is the excitation force.
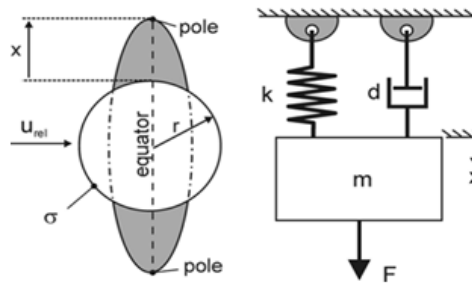

Figure 14: Sketch of deformed fuel drop and of the forced damped spring-mass system utilized in the TAB model [2].

The damping coefficient, d, depends on the viscous forces within the droplet (energy dissipation), while the spring coefficient, k, depends on surface tension forces (which act towards minimizing the droplet distortion). The excitation force F corresponds to the aerodynamic forces, which are proportional to the surrounding gas density. Specifically, the individual terms of Equation 1 are modeled as follows:

Damping term: $\dfrac{d}{m} = \dfrac{5 \cdot \mu_l}{\rho_l \cdot r^2}$ (2)

Spring term: $\dfrac{k}{m} = \dfrac{8 \cdot \sigma_l}{\rho_l \cdot r^3}$ (3)

Excitation term: $\dfrac{F}{m} = \dfrac{2 \cdot \rho_g \cdot u_{rel}^2}{3 \cdot \rho_l \cdot r^2}$ (4)

where, μ_l is the fuel dynamic viscosity, ρ_l is the fuel density, σ is the fuel surface tension, ρ_g is the density of the surrounding gas, and u_{rel} is the relative velocity between the droplet and the surrounding gas.

The modifications introduced in CAB [12] concern the IDSD, the initial conditions regarding the deformation velocity, and the calculation of the number and size of the product droplets, resulting from breakup. More precisely, the initially injected droplets follow a power law IDSD, accounting for droplet surface stripping close to the nozzle exit:

$$g(r) = \frac{n+4}{r_0} \cdot \left(\frac{r}{r_0}\right)^{n+3} \qquad (5)$$

where, n is a model constant, r is the droplet radius, and r_0 is the nozzle radius.

Further, the choice of the initial deformation velocity takes into account that the first breakup of an injected drop occurs at a certain distance from the nozzle tip, which is based on the following experimentally determined formula:

$$L = u_0 t_{bu} = C_\lambda d_0 \sqrt{\frac{\rho_l}{\rho_g}} \quad (6)$$

where, u_0 is the jet exit velocity, t_{bu} is the drop break-up time, C_λ is a model constant depending on the nozzle design, d_0 is the nozzle diameter, ρ_l is the liquid fuel density and ρ_g is the density of the surrounding gas.

The product droplet number and size is related to the breakup time via a proportionality constant, K_{bu}, which accounts for three regimes, namely, bag, stripping and catastrophic breakup. It is noted that K_{bu} is specified through the droplet oscillation frequency, ω (Equation 8), and the Weber number, We, as follows:

$$K_{bu} = \begin{cases} k_1\omega, if\ We \leq We_{b,s}\ (bag\ breakup) \\ k_2\omega\sqrt{We}, if\ We_{b,s} < We < We_{s,c}\ (stripping\ breakup) \\ k_3\omega We^{3/4}, if\ We > We_{s,c}\ (catastrophic\ breakup) \end{cases} \quad (7)$$

$$\omega^2 = \frac{8\sigma}{\rho_l r^3} - \frac{25\mu_l^2}{4\rho_l^2 r^4} \quad (8)$$

where, k_1, k_2 and k_3 are model constants, We is the Weber number of the drop before breakup, $We_{b,s}$ is the transition Weber number between bag and stripping breakup, and $We_{s,c}$ is the transition Weber number between stripping and catastrophic breakup. The model constants k_1, k_2 and k_3 are based on experimental measurements of drop size, and the transition between the individual break-up regimes, as expressed by K_{bu}, is considered continuous. Consequently, only the value k_1 needs to be determined.

8. Appendix 2: The KHRT Spray Model

The KHRT spray model [15] is a combination of two instability analysis for liquid jets; the Kelvin-Helmholtz and the Rayleigh-Taylor instabilities. The KH instability is used for the primary break-up simulation and the RT instability is used for the secondary break-up simulation.

The perturbation growth rate Λ_{KH} the wavelength Ω_{KH}, the break-up time and the droplet diameter are determined as follows:

$$\Lambda_{KH} = 9.02 \frac{r\left(1+0.45Oh^{0.5}\right)\left(1+0.4Ta^{0.7}\right)}{\left(1+0.865We^{1.67}\right)^{0.6}} \quad \textbf{(9)}$$

$$\Omega_{KH} = \frac{\left(0.34+0.38We^{3/2}\right)}{(1+Oh)(1+1.4Ta^{0.6})}\sqrt{\frac{\sigma}{\rho_d r^3}} \quad \textbf{(10)}$$

$$r_c = B_0\Lambda_{KH} \quad \textbf{(11)}$$

$$\tau_{KH} = \frac{3.72B_1 r}{\Omega_{KH}\Lambda_{KH}} \quad \textbf{(12)}$$

where, We is the Weber number, Oh, is the Ohnesorge number, Ta, is the Taylor number, σ is the surface tension, ρ is the density, r is the drop radius, B_0 and B_1 are the Kelvin-Helmholtz model constant.

The rate of change of the radius of the parent parcel is calculated as follows:

$$\frac{dr}{dt} = \frac{r-r_c}{\tau_{KH}} \quad \textbf{(13)}$$

In the RT model, the frequency of the fastest growing wave Λ_{RT} is given by

$$\Lambda_{RT} = 2\pi C_{RT}\sqrt{\frac{3\sigma}{g_t(\rho_l-\rho_g)}} \quad \textbf{(14)}$$

Where g_t and C_{RT} are the acceleration in the direction of travel, and the constant of RT model.